Research Square

Preprints are preliminary reports that have not undergone peer review.
They should not be considered conclusive, used to inform clinical practice,
or referenced by the media as validated information.

Self-Cleaning HGN–$CoTiO_3$-TiO_2-PVDF Ultrafiltration Membranes for Antibiotic Removal and Fouling Mitigation in Wastewater Treatment

Mahendra Kumar
Khalifa University of Science and Technology
Mohammad Faraz
Khalifa University of Science and Technology
Hanaa Hegab
Khalifa University of Science and Technology
Aya F. Aboukhater
Khalifa University of Science and Technology
Mariam Ouda
Khalifa University of Science and Technology
Habiba Alsafar
Khalifa University of Science and Technology
Rahul R. Nair
National Graphene Institute, Henry Royce Institute, The University of Manchester
Shadi W. Hasan
shadi.hasan@ku.ac.ae

Khalifa University of Science and Technology

Article

Keywords: HGN–$CoTiO_3$/TiO_2 heterostructure, Antibiotic photodegradation, Hospital wastewater treatment, Self-cleaning membranes, Hybrid photocatalytic membranes

Posted Date: October 29th, 2026

DOI: https://doi.org/10.21203/rs.3.rs-11349651/v1

License: This work is licensed under a Creative Commons Attribution 4.0 International License.
Read Full License

Additional Declarations: No competing interests reported.

Self-Cleaning HGN–$CoTiO_3$-TiO_2-PVDF Ultrafiltration Membranes for Antibiotic Removal and Fouling Mitigation in Wastewater Treatment

Mahendra Kumar[1,2], Mohammad Faraz[1,2], Hanaa Hegab[1,3], Aya F. Aboukhater[1,2], Mariam Ouda[1,2], Habiba Alsafar[4,5], Rahul R. Nair[6], Shadi W. Hasan[1,2]*

[1]Center for Membranes and Advanced Water Technology (CMAT), Khalifa University of Science and Technology, PO Box 127788, Abu Dhabi, United Arab Emirates

[2]Department of Chemical and Petroleum Engineering, Khalifa University of Science and Technology, PO Box 127788, Abu Dhabi, United Arab Emirates

[3]Faculty of Engineering, Higher Colleges of Technology, Abu Dhabi, United Arab Emirates

[4]Department of Biomedical Engineering and Biotechnology, Khalifa University of Science and Technology, PO Box 127788, Abu Dhabi, United Arab Emirates

[5]Center for Biotechnology (BTC), Khalifa University of Science and Technology, PO Box 127788, Abu Dhabi, United Arab Emirates

[6]National Graphene Institute, Henry Royce Institute and Department of Chemical Engineering, The University of Manchester, Manchester, United Kingdom

**Corresponding Author: shadi.hasan@ku.ac.ae*

Abstract

Antibiotic residues released from hospital effluents contribute to environmental contamination and accelerate antimicrobial resistance, highlighting the need for membrane technologies capable of simultaneously achieving pollutant removal and fouling mitigation. Herein, a multifunctional photocatalytic ultrafiltration membrane was developed by incorporating a holey graphene (HGN)–$CoTiO_3$/TiO_2 heterostructure into a poly(vinylidene fluoride) (PVDF) matrix through the non-solvent induced phase separation (NIPS) method. The HGN–$CoTiO_3$/TiO_2 heterostructure exhibited enhanced optical absorption together with improved charge separation and interfacial electron transport, resulting in superior photocatalytic activity toward tetracycline (TCL) and ciprofloxacin (CFL). The optimized heterostructure achieved 99% TCL and 96% CFL removal in antibiotic-spiked hospital wastewater under 365 nm UV irradiation. Incorporation of HGN–$CoTiO_3$/TiO_2 into PVDF significantly improved membrane hydrophilicity and surface charge, leading to ~98% humic acid rejection together with

excellent antifouling behaviour and UV-assisted flux recovery. Under static photocatalytic conditions, the optimized membrane (MTG2) achieved approximately 97–98% TCL removal, demonstrating effective photocatalytic self-cleaning. The enhanced membrane performance is attributed to the synergistic combination of membrane separation and photocatalytic oxidation enabled by the HGN–$CoTiO_3$/TiO_2 heterostructure. This work provides an effective strategy for developing photocatalytic self-cleaning ultrafiltration membranes for the treatment of antibiotic-contaminated hospital wastewater.

Keywords: HGN–$CoTiO_3$/TiO_2 heterostructure; Antibiotic photodegradation; Hospital wastewater treatment; Self-cleaning membranes; Hybrid photocatalytic membranes.

1. Introduction

Antibiotics are extensively used to treat bacterial infections in humans and animals, with global consumption projected to increase by 67% by 2030. Wastewater treatment plants, hospital effluents, sewage discharge, agricultural runoff, and improper pharmaceutical disposal contribute to the continuous release of antibiotic residues into aquatic environments. The presence of these compounds poses significant ecological and public health risks, particularly through the proliferation of antibiotic-resistant bacteria and resistance genes[1-3]. Among commonly detected antibiotics, CFL and TCL are frequently identified in wastewater effluents, where their persistence exacerbates antimicrobial resistance concerns[4,5]. These challenges underscore the urgent need of efficient and sustainable treatment technologies capable for removing antibiotic contaminants from wastewater streams.

Conventional approaches, including adsorption, oxidation, biodegradation, and bio-electrochemical systems, have applied for the treatment of antibiotic-contaminated wastewater[1,6-9]. However, their effectiveness is often limited by the complex molecular structures, chemical stability, and low biodegradability of antibiotics[3,8]. Advanced oxidation processes (AOPs) have therefore gained considerable attention due to their ability to generate highly reactive species capable of degrading organic pollutants[2,3]. Among AOPs, photocatalysis has emerged as a promising and sustainable strategy for antibiotic remediation in water systems[3,5,10]. Various semiconductor nanomaterials, including ZnO, V_2O_5, $LiNbO_3$, TiO_2, CdS, ZnS, and Fe_3O_4, have explored for photocatalytic water treatment applications. Nevertheless, widely used photocatalysts such as TiO_2 suffer from intrinsic limitations, including wide bandgap energy, low quantum efficiency,

and rapid recombination of photogenerated electron–hole pairs, which restrict their practical performance[3,11].

To overcome these limitations, strategies such as heteroatom doping, morphology engineering, surface modification, and heterostructure construction have been employed to enhance charge separation and redox efficiency[4,12,13]. For instance, Ag-doped ZnO nanocomposites synthesized via a sol–gel method demonstrated improved visible-light photocatalytic degradation of CFL and TCL due to enhanced electron–hole separation compared to pristine ZnO[4]. In addition to doping, constructing heterostructured interfaces between semiconductors has proven effective in promoting internal electric field formation, accelerating charge carrier separation, and facilitating interfacial charge transfer under light irradiation[10,14,15]. Titanium-based perovskite metal titanates ($MTiO_3$; M = Co, Ni, Zn, Fe) have attracted attention as photoactive materials. Binary heterostructures such as $FeTiO_3/TiO_2$, $CoTiO_3/TiO_2$, $CoTiO_3$/BiOBr, $NiTiO_3/TiO_2$, and $ZnTiO_3/TiO_2$ have demonstrated enhanced charge separation and improved photocatalytic activity compared to TiO_2 alone under UV and visible irradiation[16-20]. For example, a C–$TiO_2/CoTiO_3$ core–shell heterostructure synthesized via MIL-125/Co calcination showed visible-light-driven CFL degradation[17]. Despite these advances, binary heterostructures often exhibit limited spatial charge separation and suboptimal redox efficiency, which can constrain their degradation performance.

Ternary heterostructured systems have therefore been developed to further enhance charge migration pathways and redox activity[21,22]. Xia et al. reported a UiO-66-NH_2/BiOCl/Bi_2S_3 ternary heterostructure that broadened visible-light absorption and enhanced TCL degradation through improved photogenerated carrier separation[22]. More recently, the integration of semiconductor photocatalysts with two-dimensional (2D) materials; such as g-C_3N_4, graphene (GN), reduced graphene oxide (rGO), $Ti_3C_2T_x$, and boron nitride (BN); has provided an effective approach for constructing ternary heterostructures with accelerated interfacial charge transfer and enhanced photocatalytic performance[14,23-27]. For example, TiO_2/ZrO_2/g-C_3N_4 nanocomposites exhibited improved antibiotic degradation due to heterojunction formation and rapid charge transport[23], while TiO_2/g-C_3N_4/BN composites promoted reactive oxygen species (ROS) generation, enabling efficient TCL degradation via $\bullet O_2^-$, h^+, and •OH pathways[25].

Among the emerging treatment technologies, photocatalytic membranes have attracted increasing attention because they integrate membrane separation within situ photocatalytic degradation, enabling simultaneous contaminant removal and fouling mitigation within a single process. Nevertheless, the practical performance of photocatalytic membranes remains limited by the insufficient charge separation and poor interfacial electron transport of conventional photocatalysts, highlighting the need for advanced heterostructured photocatalytic materials. Beyond powder photocatalysis, 2D material-enabled heterostructures have been increasingly explored in the development of self-cleaning photocatalytic hybrid membranes for water treatment[27-30]. However, holey graphene (HGN)-integrated heterostructured photocatalysts remain comparatively underexplored for simultaneous antibiotic degradation and antifouling membrane applications. HGN offers distinct advantages, including high specific surface area, excellent electrical conductivity, reduced aggregation, and scalable production, making it a promising conductive bridge and structural modifier for advanced photocatalytic systems[31]. The incorporation of HGN into ternary heterostructures may therefore enhance charge separation, facilitate electron transport, and improve interfacial reactivity. Despite these advances, most studies have primarily focused on suspended photocatalysts, whereas the incorporation of conductive ternary heterostructures into ultrafiltration membranes for simultaneous antibiotic degradation and antifouling has received comparatively limited attention.

In this work, a ternary HGN–$CoTiO_3$/TiO_2 heterostructure was synthesized through a hydrothermal approach using HGN as a conductive scaffold to promote interfacial electron transport and suppress charge recombination. The optimized heterostructure was subsequently incorporated into a poly(vinylidene fluoride) (PVDF) ultrafiltration membrane via the NIPS process to fabricate a photocatalytic self-cleaning membrane. The developed membranes were systematically evaluated in terms of physicochemical properties, permeability, antifouling behaviour, UV-assisted self-cleaning, and photocatalytic degradation of TCL and CFL. Finally, the applicability of the proposed system was demonstrated using antibiotic-spiked hospital wastewater, providing an effective strategy for membrane-based treatment of antibiotic-contaminated wastewater.

2. Materials and Methods

Photocatalytic mixed-matrix PVDF ultrafiltration membranes containing HGN–$CoTiO_3/TiO_2$ nanocomposites were fabricated and evaluated for membrane transport, fouling mitigation, and photocatalytic performance. Detailed informations associated with materials, nanocomposite synthesis, membrane fabrication, characterization techniques, photocatalytic measurements, electrochemical analyses, and membrane testing protocols is provided in the Electronic Supplementary Information (ESI). A schematic presentation for $CoTiO_3/TiO_2$ nanocomposites is displayed in **Fig. 1.**

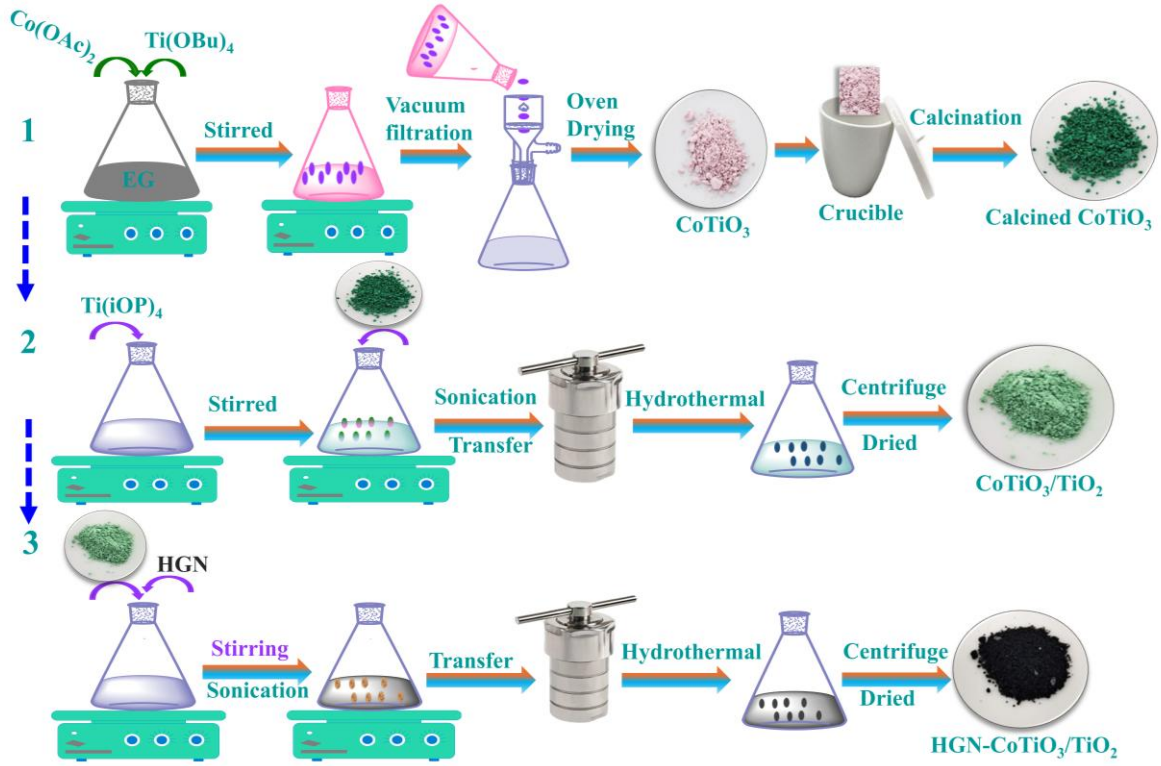


Fig. 1. Schematic illustration for synthesis of HGN-$CoTiO_3/TiO_2$ nanocomposite via sol-gel reaction, calcination and hydrothermal treatment.

3. Results and Discussion

3.1. Physicochemical characteristics of the HGN–$CoTiO_3/TiO_2$ nanocomposite

The crystal structure of $CoTiO_3$, $CoTiO_3/TiO_2$, and HGN–$CoTiO_3/TiO_2$ was examined by XRD **(Fig. 2a,b)**. Based on the XRD results, $CoTiO_3$ calcined at 700°C exhibited the highest crystallinity and was therefore selected for subsequent composite synthesis. The characteristic diffraction peaks located at 2θ = 24.2°, 33.1°, 35.7°, 40.8°, 49.2°, 53.6°, 57.1°, 62.0°, and 63.8° were indexed to the (012), (104), (110), (113), (024), (116), (018), (214), and (300) planes of ilmenite $CoTiO_3$[32,33]. Following hydrothermal coupling,

additional reflections at 25.7°, 38.2°, 48.4°, 55.1°, and 63.0° corresponding to the (101), (004), (200), (211), and (204) planes confirmed the formation of anatase TiO_2. The diffraction pattern of HGN–$CoTiO_3$/TiO_2-30 retained the characteristic reflections of both $CoTiO_3$ and TiO_2 without the appearance of secondary crystalline phases, indicating that HGN incorporation preserved the crystal structure of the heterojunction. A weak diffraction peak centred at approximately 26.8° was assigned to the (002) plane of HGN, confirming its successful incorporation into the composite. Similar diffraction patterns were obtained for HGN-$CoTiO_3$/TiO_2-10 and HGN–$CoTiO_3$/TiO_2-20 (**Fig. S3a**), demonstrating that varying the HGN loading did not alter the crystalline structure of the heterojunction.

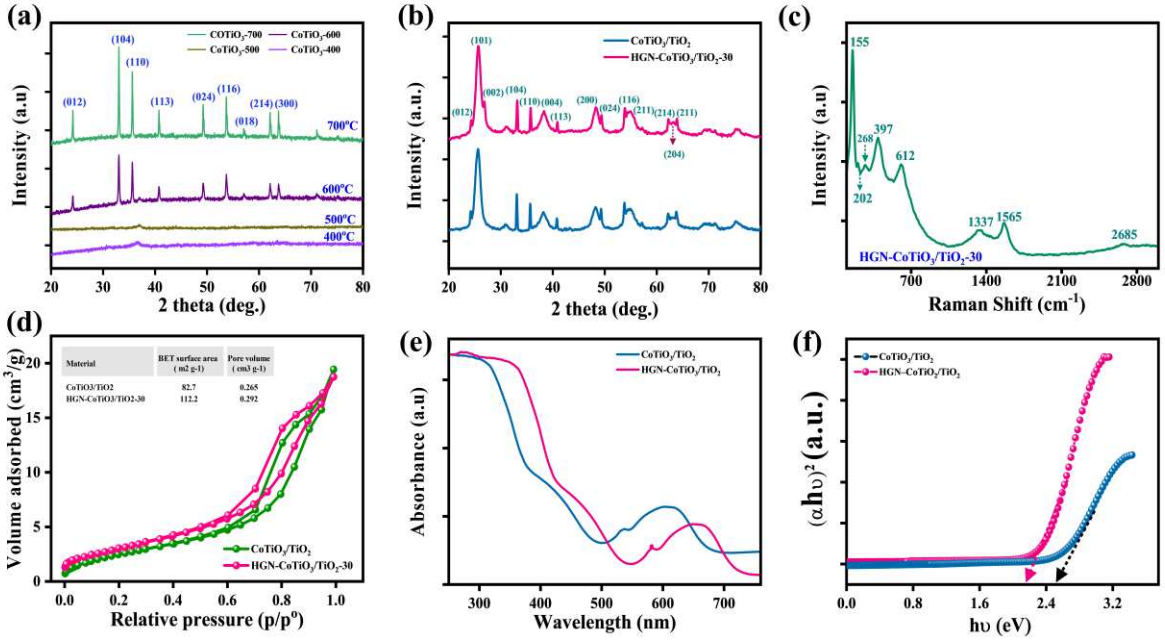


Fig. 2. Physicochemical characteristics of the HGN–$CoTiO_3$/TiO_2 heterostructure: (a) XRD patterns of $CoTiO_3$, (b) $CoTiO_3$/TiO_2, and HGN–$CoTiO_3$/TiO_2-30, (c) Raman spectra of $CoTiO_3$/TiO_2 and HGN–$CoTiO_3$/TiO_2-30, (d) N_2 adsorption–desorption isotherms (inset: BET surface area and pore volume), (e) UV–Vis diffuse reflectance spectra (DRS) and (f) Kubelka–Munk transformed Tauc plots for estimation of the apparent optical band gap.

The Raman spectra **(Fig. 2c & Fig. S4)** confirmed the successful formation of the HGN–$CoTiO_3$/TiO_2 heterostructure. $CoTiO_3$/TiO_2 exhibited characteristic Raman bands at 155, 202, 270, 400, and 607 cm^{-1}, due to Ti–O lattice vibrations of the semiconductor framework[34]. The characteristic bands of $CoTiO_3$ are not clearly resolved because of its relatively low concentration in the heterostructure. Following HGN incorporation, the

composite retained the characteristic D, G, and 2D bands at ~1337, 1565, and 2685 cm^{-1}, respectively[34,35]. The coexistence of the graphitic carbon bands together with Ti–O vibrational modes confirm the integration of HGN, while preserved the crystal structure of the $CoTiO_3/TiO_2$ heterojunction. N_2 adsorption–desorption isotherms exhibited type-IV isotherms with H3 hysteresis loops in the relative pressure range of 0.6–1.0 (P/P_0) **(Fig. 2d)**, confirming the formation of mesoporous $CoTiO_3/TiO_2$ and HGN–$CoTiO_3/TiO_2$[36]. The porous structure of $CoTiO_3/TiO_2$ was well preserved after HGN incorporation. Furthermore, BET surface area and pore volume were increased from 82.7 $m^2\ g^{-1}$ and 0.265 $cm^3\ g^{-1}$ for $CoTiO_3/TiO_2$ to 112.2 $m^2\ g^{-1}$ and 0.292 $cm^3\ g^{-1}$ for HGN–$CoTiO_3/TiO_2$-30. The increased surface area and pore volume provide more accessible sites for adsorption and photocatalytic reactions. The UV–Vis diffuse reflectance spectra **(Fig. 2e,f)** show a broad absorption of HGN throughout the UV–visible region without distinct semiconductor absorption edge, consistent with its conductive graphitic structure. In contrast, HGN–$CoTiO_3/TiO_2$-30 displays improved optical absorption with characteristic bands centred at ~ 535 and 610 nm, which are attributed to $Co^{2+}\rightarrow Ti^{4+}$ charge-transfer and Co^{2+} d–d electronic transitions[32,37]. Absorption < 500 nm originates from $O^{2-}\rightarrow Ti^{4+}$ charge-transfer transitions associated with $TiO_2/CoTiO_3$ heterojunction [37,38]. The apparent optical band gap decreased from **2.42 eV** for $CoTiO_3/TiO_2$ to **2.22 eV** for HGN–$CoTiO_3/TiO_2$-30, indicating enhanced light harvesting and stronger electronic interaction following HGN incorporation.

3.2. Charge-transfer characteristics of the HGN–$CoTiO_3/TiO_2$ nanocomposite

The PL spectra of $CoTiO_3/TiO_2$ and HGN-$CoTiO_3/TiO_2$-30 are presented in **Fig. 3a**. Compared with $CoTiO_3/TiO_2$, HGN-$CoTiO_3/TiO_2$-30 exhibited markedly lower emission intensity, indicating suppressed radiative recombination of photogenerated electron–hole pairs. The reduced PL intensity suggests the improved charge separation within the heterostructure after HGN incorporation[39,40]. The transient photocurrent responses of $CoTiO_3/TiO_2$ and HGN-$CoTiO_3/TiO_2$-30 are displayed in **Fig. 3b**. HGN-$CoTiO_3/TiO_2$-30 generated a higher and more stable photocurrent response than $CoTiO_3/TiO_2$ during the repeated light on/off cycles, indicating more efficient separation and transport of photogenerated charge carriers. The enhanced photocurrent confirms that HGN provides an effective conductive pathway for rapid electron migration across the heterojunction[41]. The Nyquist plots shown in **Fig. 3c** further confirm the improved charge-transfer

characteristic of the heterostructures. Compared with $CoTiO_3/TiO_2$, HGN–$CoTiO_3/TiO_2$-30 revealed a smaller semicircle diameter, signifying lower interfacial charge-transfer resistance. The reduced impedance is consistent with the PL and photocurrent results, demonstrating that HGN facilitates faster electron transport and suppresses charge recombination within the heterostructure[42].

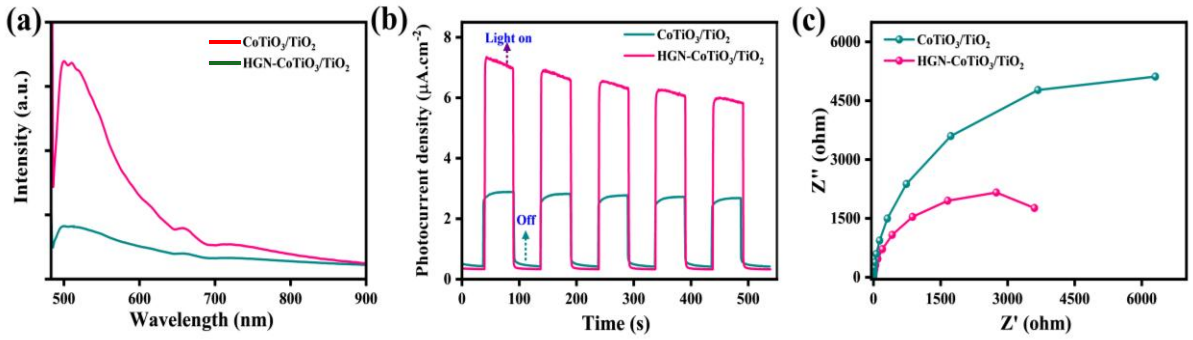


Fig. 3. Charge-transfer characteristics of $CoTiO_3/TiO_2$ and HGN–$CoTiO_3/TiO_2$-30: (a) Photoluminescence (PL) spectra, (b) Transient photocurrent responses under intermittent UV irradiation and (c) Electrochemical impedance spectroscopy (EIS) Nyquist plots.

3.3. Morphological and surface chemical characterization of the HGN–$CoTiO_3/TiO_2$ nanocomposite

The morphology of HGN, $CoTiO_3/TiO_2$, and HGN–$CoTiO_3/TiO_2$ was examined by SEM and TEM (**Fig. 4**). HGN exhibited a porous and corrugated sheet-like texture (**Fig. 4a, d**). $CoTiO_3/TiO_2$ consisted of agglomerated quasi-spherical nanoparticles, while the corresponding TEM image revealed well-defined lattice fringes, confirming the crystalline characteristic of the heterostructure (**Fig. 4b, e**). Following hydrothermal synthesis, HGN-$CoTiO_3/TiO_2$-30 displayed a rough and compact surface with uniformly distributed $CoTiO_3/TiO_2$ nanoparticles over the HGN sheets (**Fig. 4c**). The TEM image further revealed intimate interfacial intacted HGN and $CoTiO_3/TiO_2$ (**Fig. 4f**), confirming the successful formation of the HGN-$CoTiO_3/TiO_2$ nanocomposites.

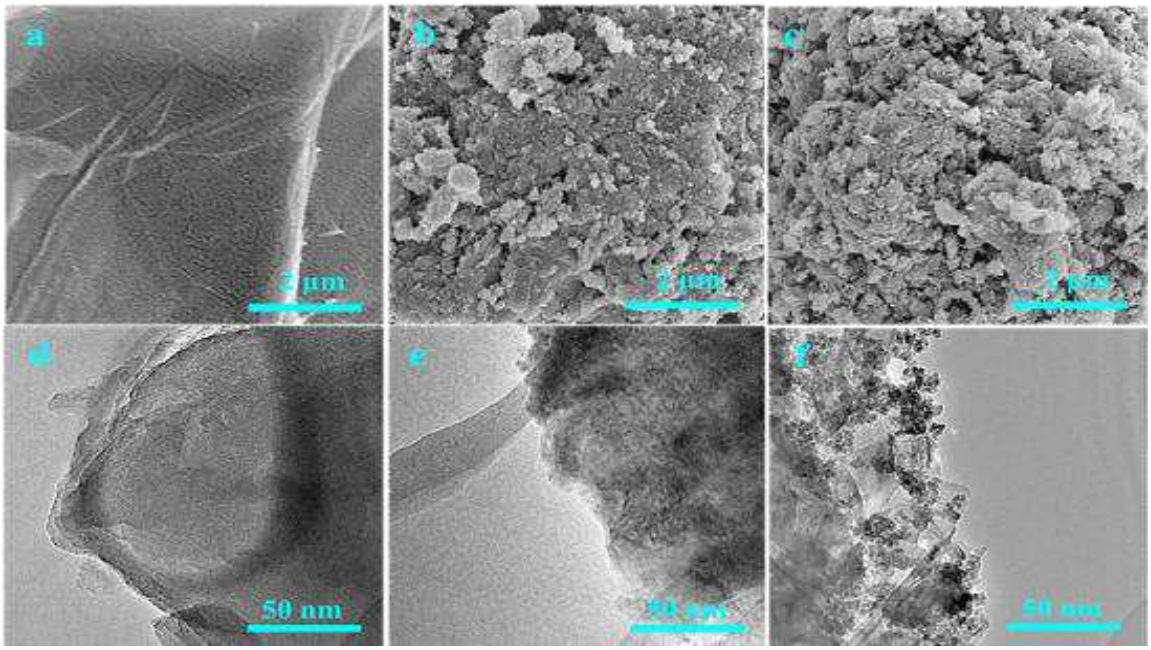


Fig. 4. Morphological characterization of the HGN–$CoTiO_3/TiO_2$ heterostructure: (a–c) SEM images and TEM images of HGN (a, d), $CoTiO_3/TiO_2$ (b, e), and (c, f) HGN-$CoTiO_3/TiO_2$-30.

The surface chemical composition analysed by X-ray photoelectron spectroscopy (**Fig. 5 and Fig. S3d**).

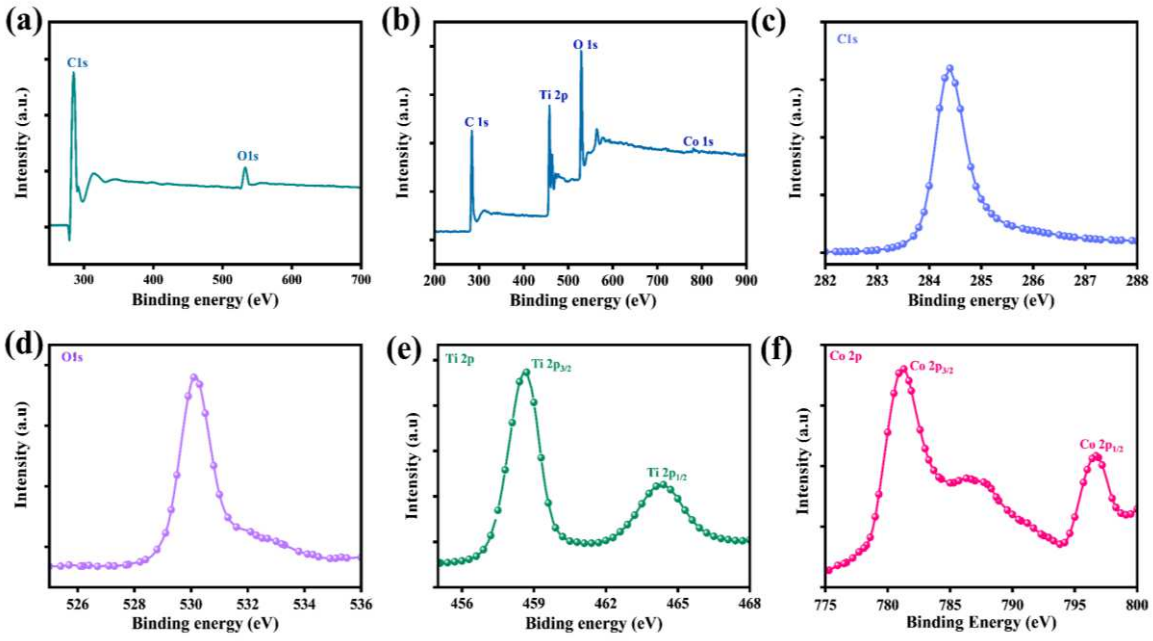


Fig. 5. Surface chemical characterization of HGN and HGN–$CoTiO_3/TiO_2$-30 by X-ray photoelectron spectroscopy (XPS): (a, b) Survey spectra of HGN and HGN-$CoTiO_3/TiO_2$-

30, respectively. High-resolution XPS spectra of (c) C 1s, (d) O 1s, (e) Ti 2p, and (f) Co 2p for HGN-$CoTiO_3/TiO_2$-30.

The survey spectra confirmed the presence of C, O, Co, and Ti in HGN-$CoTiO_3/TiO_2$-30, whereas only C and O signals were observed for HGN (**Fig. 5a, b**). The high-resolution C 1s spectrum of HGN-$CoTiO_3/TiO_2$-30 was dominated by the sp^2 carbon peak at 284.2 eV, confirming successful HGN incorporation (**Fig. 5c**). The O 1s spectrum exhibited lattice oxygen together with surface oxygen-containing species (**Fig. 5d**). The Ti 2p peaks centred at 458.6 and 464.3 eV with a spin–orbit splitting of ~ 5.7 eV confirmed the presence of Ti^{4+} (**Fig. 5e**), while the Co 2p peaks located at 781.2 and 796.7 eV with a separation of approximately 15.5 eV were assigned to Co^{2+} (**Fig. 5f**), confirming the formation of the $CoTiO_3/TiO_2$ heterostructure[17,37,43].

3.4 Effect of HGN–$CoTiO_3/TiO_2$ nanocomposites incorporation on membrane properties

The influence of HGN–$CoTiO_3/TiO_2$ incorporation on membrane morphology and physicochemical properties was investigated using hybrid PVDF membranes containing different nanocomposite loadings. Membrane porosity (ε) increased progressively for MTG0 to MTG1 and subsequently decreased at higher nanocomposite loading (MTG2) **(Table 1)**.

Table 1. Porosity (ε, %), water contact angle (WCA, °), surface free energy change (ΔG_{SL}, mJ m^{-2}), surface zeta potential (ζ, mV), tensile strength (MPa), and elongation at break (%) of pristine and hybrid membranes (mean ± standard deviation).

Membrane	ε (%)	WCA (°)	ΔG_{SL} (mJ m^{-2})	ζ (mV)	Tensile Strength (MPa)	Tensile stress (%)
MTG0	52.1±1.2	78.1±1.1	88.1±1.2	-12.2±0.6	1.6±0.2	16.4±0.7
MTG05	58.7±1.4	72.3±1.0	95.1±1.3	-13.9±0.7	1.2±0.2	24.6±1.1
MTG1	65.4±1.6	65.2±0.9	103.2±1.4	-15.8±0.8	1.1±0.2	50.6±2.1
MTG2	60.3±1.4	58.4±0.8	110.1±1.5	-18.7±0.9	1.3±0.4	65.4±2.3

The initial increase in ε is attributed to improved solvent–non-solvent exchange during phase inversion resulting from the enhanced hydrophilicity and uniform dispersion of HGN–$CoTiO_3/TiO_2$ within the polymer blend solution[28,44,45]. In contrast, a slight reduction

in ε for MTG2 is associated with increased casting-solution viscosity and partial nanocomposite agglomeration, which retard phase inversion rate and suppress macropore formation[28,46].

The surface morphology of the membranes is presented in **Fig. 6a–e**. All membranes exhibited asymmetric porous structures typical of phase-inverted PVDF membranes.

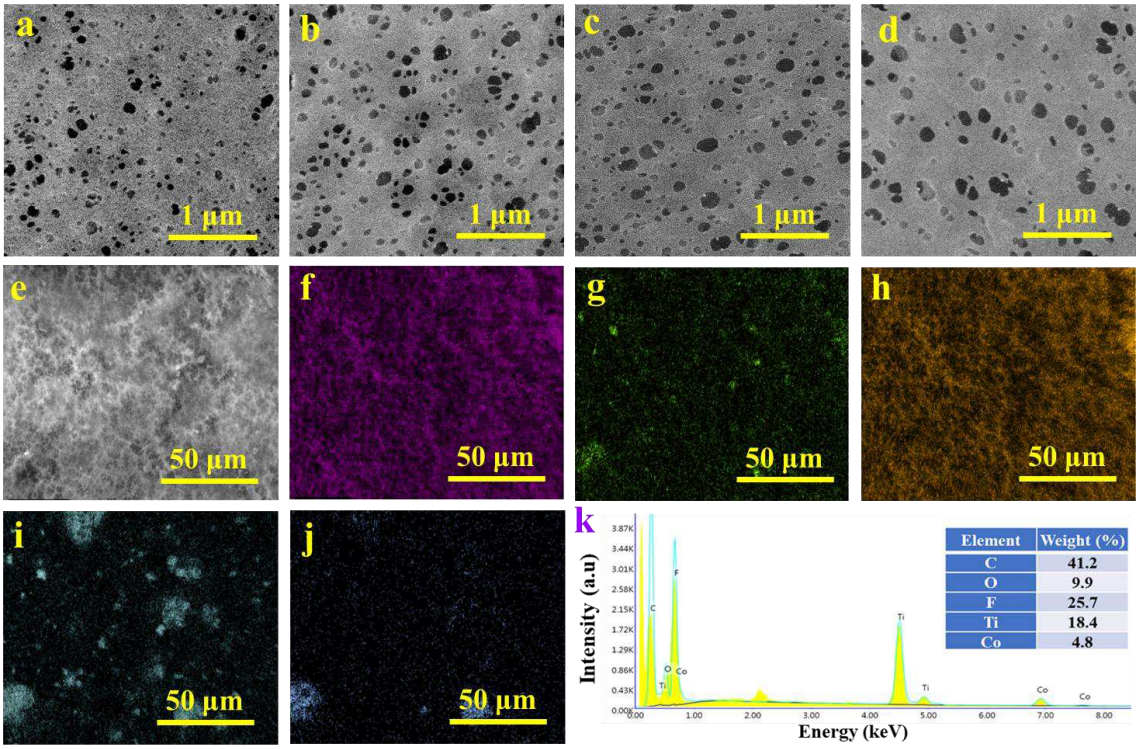


Fig. 6. Morphological characterization of pristine and HGN–$CoTiO_3$/TiO_2/PVDF hybrid membranes: (a–d) Surface SEM images of MTG0, MTG05, MTG1, and MTG2, (e) Higher-magnification SEM image of MTG2, (f–j) SEM-EDX elemental mapping of MTG2 for C, O, F, Ti, and Co and (k) Corresponding SEM–EDX spectrum of the membrane MTG2.

Compared with MTG0 (**Fig. 6a**), the hybrid membranes (**Fig. 6b–d**) maintained a similar porous morphology, although pore density gradually decreased and pore size increased slightly with increasing nanocomposite loading. A higher magnification image of MTG2 (**Fig. 6e**) further reveals the rough membrane surface resulting from the incorporation of HGN-$CoTiO_3$/TiO_2. The corresponding SEM–EDX elemental mapping (**Fig. 6f–j**) confirmed the homogeneous distribution of C, O, F, Ti, and Co throughout the membrane surface, while the EDX spectrum (**Fig. 6k**) verified the incorporation of HGN–$CoTiO_3$/TiO_2 within the PVDF matrix. The thermal stability and mechanical properties of

the membranes are summarized in **Table 1 & Fig. S5.** All membranes exhibited a single-step thermal degradation profile characteristic of PVDF membranes. A slight decrease in the decomposition temperature was observed after nanocomposite incorporation, whereas the residual weight increased with increasing HGN–$CoTiO_3$/TiO_2 loading because of the higher inorganic content. Tensile strength decreased only slightly after nanocomposite incorporation, while the elongation at break increased from 16.4% for MTG0 to 65.4% for MTG2, indicating improved membrane flexibility resulting from nanocomposite–polymer interactions[47,48]. Surface wettability and surface charge were significantly influenced by HGN–$CoTiO_3$/TiO_2 incorporation (Table 1). The water contact angle decreased from 78.1° for MTG0 to 58.4° for MTG2, indicating enhanced membrane hydrophilicity. Similarly, the surface zeta potential became progressively more negative, reaching −18.7 mV for MTG2 because of the introduction of oxygen-containing functional groups together with the negatively charged HGN framework. The increase in surface free energy further supports the improved hydrophilic nature of the hybrid membranes, which is expected to facilitate water transport and reduce membrane fouling during filtration[30,44,49].

3.5. Photocatalytic performance of the optimized HGN–$CoTiO_3$/TiO_2-30 nanocomposite

Different HGN–$CoTiO_3$/TiO_2 compositions (10, 20 and 30 wt.%) were initially evaluated to optimize the photocatalytic performance of the nanocomposites. As shown in **Fig. S6e**, HGN–$CoTiO_3$/TiO_2-30 exhibited the highest photocatalytic activity toward both TCL and CFL and was therefore selected for all subsequent photocatalytic and membrane investigations. The photocatalytic performance of HGN-$CoTiO_3$/TiO_2-30 was further evaluated under UV irradiation. The corresponding UV–Vis spectra recorded during adsorption and photocatalytic degradation are provided in **Fig. S6**. The temporal variation of the normalized concentration (C_t/C_o) for TCL and CFL is presented in **Fig. 7a**. HGN–$CoTiO_3$/TiO_2-30 exhibited rapid degradation of both antibiotics throughout the irradiation period, with TCL degrading faster than CFL under identical experimental conditions.

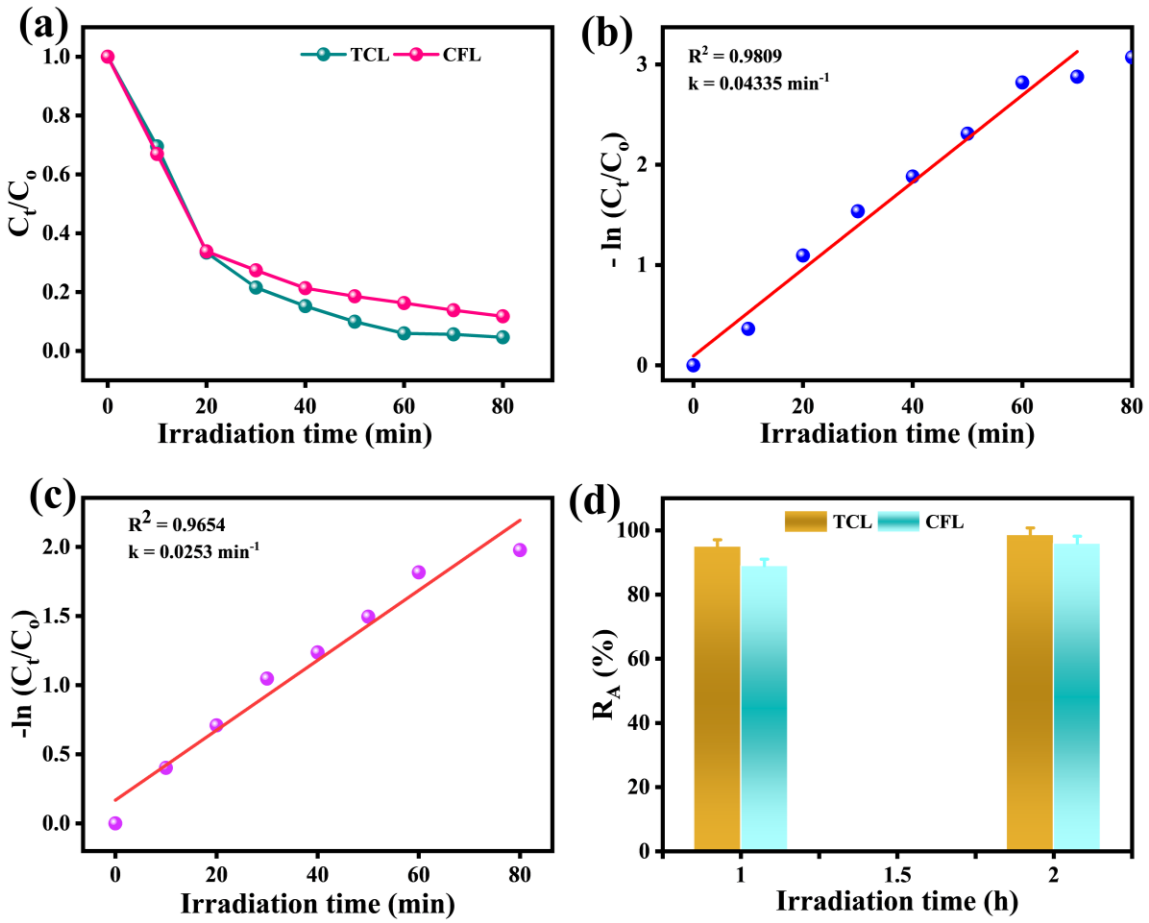


Fig. 7. Photocatalytic performance of the optimized HGN-$CoTiO_3/TiO_2$-30 heterostructure: (a) Normalized concentration (C_t/C_o) vs time profiles of TCL and CFL under UV irradiation, (b) Pseudo-first-order kinetic plots for TCL, (c) Pseudo-first-order kinetic plots for CFL and (d) Photocatalytic removal of antibiotics from spiked hospital wastewater (HWW).

The different degradation behaviours are attributed to differences in the molecular structure and adsorption characteristics of the two antibiotics[50-52]. The photocatalytic degradation kinetics were analysed using the pseudo-first-order kinetic model (Fig. 7b, c). Good linear relationships were obtained for both antibiotics ($R^2 > 0.965$), indicating that the degradation followed pseudo-first-order kinetics. The apparent rate constant of TCL (**k = 0.04335 min^{-1}**) was approximately 1.7 times higher than that of CFL (**k = 0.0253 min^{-1}**), confirming the faster degradation of TCL under identical irradiation conditions. The applicability of HGN–$CoTiO_3/TiO_2$-30 was further evaluated using antibiotic-spiked hospital wastewater (HWW) under UV irradiation (**Fig. 7d**). Compared with pure aqueous solutions, the degradation rate in HWW was slightly slower, requiring a longer irradiation time because of the presence of dissolved organic matter and

inorganic constituents in the wastewater matrix. Increasing the irradiation time from 1 to 2 h improved the removal efficiency from 95% to ~99% for TCL and from 90% to 96% for CFL, demonstrating the potential applicability of HGN-$CoTiO_3/TiO_2$-30 for photocatalytic treatment of antibiotic-contaminated hospital wastewater.

3.6 Photocatalytic stability and reactive species investigation

The photocatalytic stability of HGN-$CoTiO_3/TiO_2$-30 was evaluated over seven consecutive degradation cycles (**Fig. 8a**). After each cycle, the photocatalyst was recovered by vacuum filtration, thoroughly washed with deionized water, and dried at 70 °C prior to reuse. HGN–$CoTiO_3/TiO_2$-30 maintained high photocatalytic activity throughout the repeated cycles, with only minor decreases of 3.8% for TCL and 10% for CFL after the seventh cycle. The slight loss in photocatalytic activity is primarily attributed to unavoidable catalyst loss during the recovery process rather than structural deactivation. Furthermore, the XRD patterns and XPS spectra of the fresh and reused photocatalysts remained essentially unchanged (**Fig. S7d**), confirming the excellent structural stability of the HGN–$CoTiO_3/TiO_2$ heterostructure during repeated photocatalytic operation.

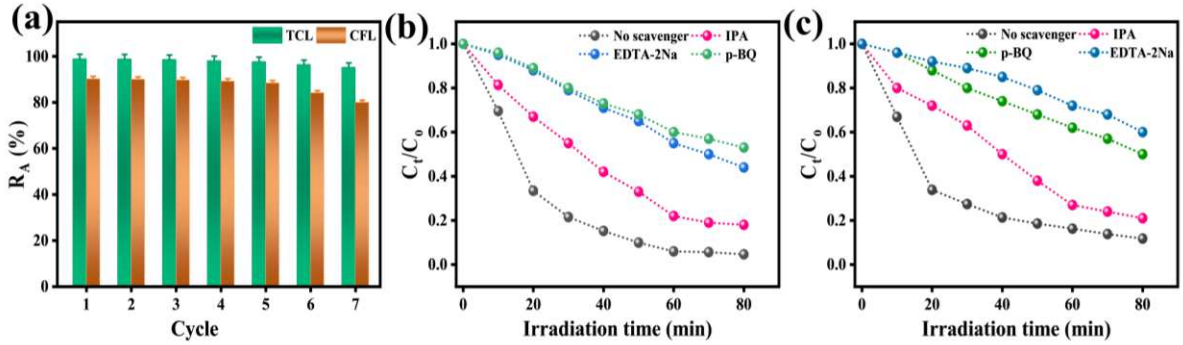


Fig. 8. Photocatalytic stability and reactive species investigation of HGN–$CoTiO_3/TiO_2$-30: (a) Photocatalytic stability over seven consecutive degradation cycles, and (b,c) Effect of IPA, BQ, and EDTA-2Na scavengers on the photocatalytic degradation of TCL and CFL.

Reactive species trapping experiments were carried out to identify the dominant reactive species involved in the photocatalytic degradation of TCL and CFL (**Fig. 8b,c**). Isopropanol (IPA), benzoquinone (BQ), and ethylenediaminetetraacetic acid disodium salt (EDTA-2Na) were employed as scavengers for hydroxyl radicals (•OH), superoxide radicals ($\bullet O_2^-$), and photogenerated holes (h^+), respectively. The addition of each scavenger reduced the photocatalytic degradation efficiency compared with the control,

confirming that multiple reactive species participated in the degradation process. For TCL, the greatest inhibition was observed in the presence of p-BQ, indicating that superoxide radicals ($\bullet O_2^-$) were the dominant reactive species. In contrast, the strongest inhibition during CFL degradation was observed after the addition of EDTA-2Na, suggesting that photogenerated holes (h^+) played the dominant role in the degradation process. These results demonstrate that the dominant reactive species depend on the target antibiotic, although both radical and hole mediated oxidation pathways contribute to the overall photocatalytic activity of HGN–$CoTiO_3$/TiO_2-30.

3.7. Membrane permeability and separation performance

Pure water flux (J_w) trends are shown in **Fig. 9a**. MTG0 exhibited J_w = 394 L m^{-2} h^{-1} bar^{-1}, while MTG05, MTG1, and MTG2 exhibited 429, 518, and 327 L m^{-2} h^{-1} bar^{-1}, respectively. The increase in J_w from MTG0 to MTG1 is consistent with increased porosity and hydrophilicity **(Table 1)**, which facilitate pore formation and water transport[27,44,49]. At 2 wt.% loading, Jw decreased sharply despite the lowest contact angle, indicating that reduced porosity (ε) dominates transport resistance in MTG2; therefore, pore-structure limitation outweighs the benefit of higher hydrophilicity. Humic acid, as a representative natural organic matter component, was selected to evaluate rejection. As expected, J_{HA} values were lower than J_w for all membranes due to HA deposition/fouling **(Fig. 9a)**. However, J_{HA} was higher for hybrid membranes than MTG0, indicating mitigated fouling upon nanocomposite incorporation. This behavior is consistent with reduced HA adhesion due to formation of a more robust surface hydration layer[49,53,54]. HA rejection (R_{HA}) increased with nanocomposite loading **(Fig. 9d)**, consistent with reduced absorbance of permeates at higher loadings **(Fig. 9b)**. MTG2 exhibited the lowest permeate absorbance and the highest rejection (~98%). The enhanced rejection is attributed to electrostatic repulsion between negatively charged HA and increasingly negative membrane surfaces **(Table 1)** as well as size/charge exclusion effects commonly governing UF removal[49,53,54]. The reduced porosity and higher ζ potential of MTG2 likely contribute to narrower hydrated pores and stronger electrostatic exclusion, collectively producing higher HA rejection.

3.8. Antifouling and UV-Assisted Self-Cleaning

Antifouling and self-cleaning performance were evaluated using flux recovery after water rinsing and subsequent UV irradiation. After water rinsing, $J_{w,pc}$ increased relative to JHA but did not recover to the original J_w, yielding limited FRR for all membranes **(Fig. 9c)**.

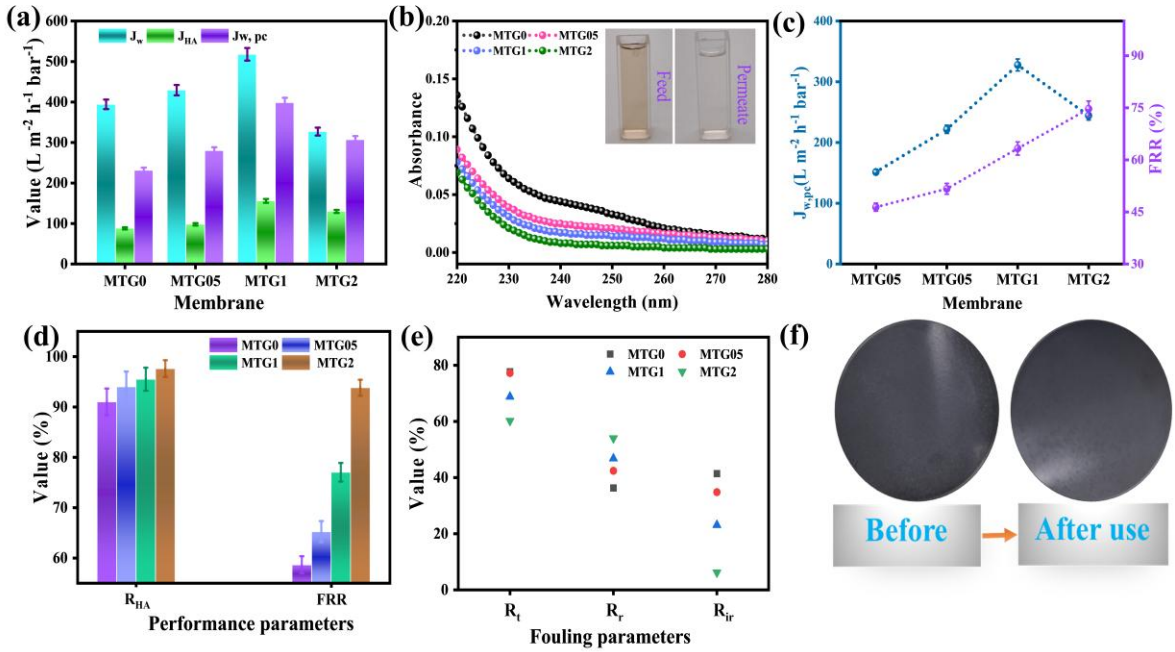


Fig. 9. (a) J_w, J_{HA}, and $J_{w,UV}$, (b) UV–Vis absorbance of HA permeates and photographs for permeate & feed, (c) $J_{w,pc}$ and FRR after water washing, (d) R_{HA} and FRR after UV-assisted cleaning, (e) R_t, R_r, and R_{ir} and (f) Photographs of MTG2 before and after use followed by UV treatment.

This indicates that water rinsing alone cannot remove strongly adhered HA or fully restore flux. To activate photocatalytic cleaning, fouled membranes were exposed to UV irradiation for 30 min. UV treatment slightly improved $J_{w,UV}$ and FRR for MTG0 due to partial degradation of surface-bound HA under high-intensity UV. In contrast, UV-treated hybrid membranes exhibited substantially improved $J_{w,UV}$ and FRR **(Fig. 9a,d)**, demonstrating effective photocatalytic self-cleaning. MTG2 achieved the highest FRR, consistent with efficient photodecomposition of strongly adhered HA enabled by the embedded photocatalyst[44,55]. Although full recovery to the original J_w was not achieved, the remaining gap likely reflects residual HA within pores and/or incomplete mineralization. Fouling mechanisms were quantified using R_t, R_r, and R_{ir} **(Fig. 9e)**. Total fouling decreased markedly after nanocomposite incorporation, following MTG2 < MTG1 < MTG05 < MTG0, indicating that increased hydrophilicity and UV-activated degradation

jointly reduce fouling accumulation. Reversible fouling increased with loading, consistent with weaker HA adhesion and improved removal of loosely attached HA via water washing. Irreversible fouling was highest for MTG0 (41.4%) and decreased progressively with nanocomposite loading, confirming suppression of strongly bound foulants and enhanced UV-assisted removal. Overall, MTG2 exhibited superior combined permeability recovery and rejection performance and compares favorably with reported photocatalytic hybrid membranes **(Table S2)**.

3.9. Membrane Photodegradation Performance for TCL Removal

Photocatalytic degradation of TCL by membranes was evaluated under static conditions using 20 ppm TCL under UV irradiation. For MTG2, the characteristic TCL absorbance peak disappeared after 180 min irradiation, and the treated solution exhibited minimal absorbance, indicating efficient TCL photodegradation **(Fig. S5c)**. The dependence of TCL removal on irradiation time is shown in **Fig. 10a.**

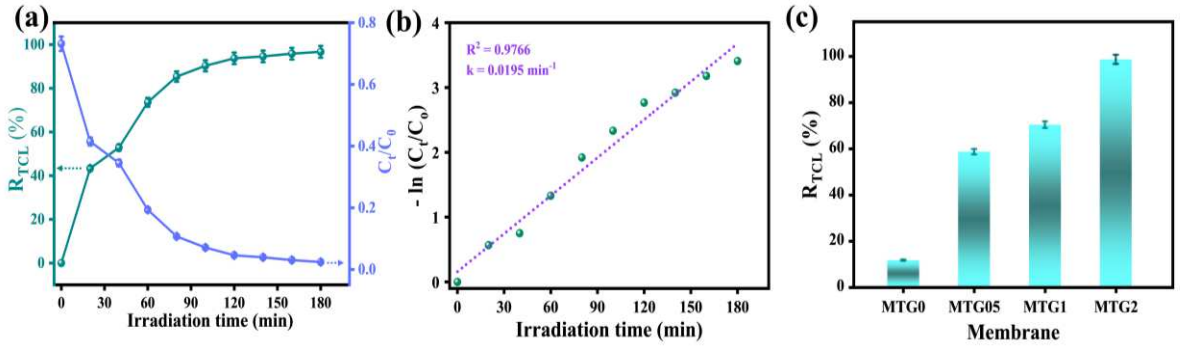


Fig. 10. (a) TCL removal efficiency of MTG2 during static photodegradation under UV irradiation. (b) First-order kinetic fit for TCL degradation using MTG2. (c) TCL removal efficiencies of MTG0 and hybrid membranes after 180 min UV irradiation.

R_{TCL} increased progressively with UV exposure, reaching ~97% removal after 180 min using MTG2. Kinetics were fitted using a first-order model, yielding $R^2 > 0.9766$ and an apparent rate constant $k = 1.95 \times 10^{-2}$ min^{-1} **(Fig. 10b)**, confirming robust first-order behavior under the tested conditions. Comparative TCL degradation across membranes is shown in **Fig. 10c**. Pristine MTG0 removed only 12% TCL after 180 min UV exposure, whereas removal increased with HGN-$CoTiO_3$/TiO_2-30 loading. RTCL increased from 58.7% to ~98% when loading increased from 0.5 to 2 wt.%, consistent with enhanced charge transfer and greater ROS generation during irradiation in the presence of the

photocatalytic nanocomposite. The final performance order was 98% (MTG2) > 70.4% (MTG1) > 59% (MTG05) > 11.7% (MTG0).

3.10 Proposed photocatalytic mechanism of the HGN–$CoTiO_3$/TiO_2 heterostructure and its role in membrane self-cleaning

Based on the structural, optical, photoelectrochemical, and reactive species trapping analyses, a photocatalytic mechanism for the HGN–$CoTiO_3$/TiO_2 heterostructure is proposed (**Fig. 11**).

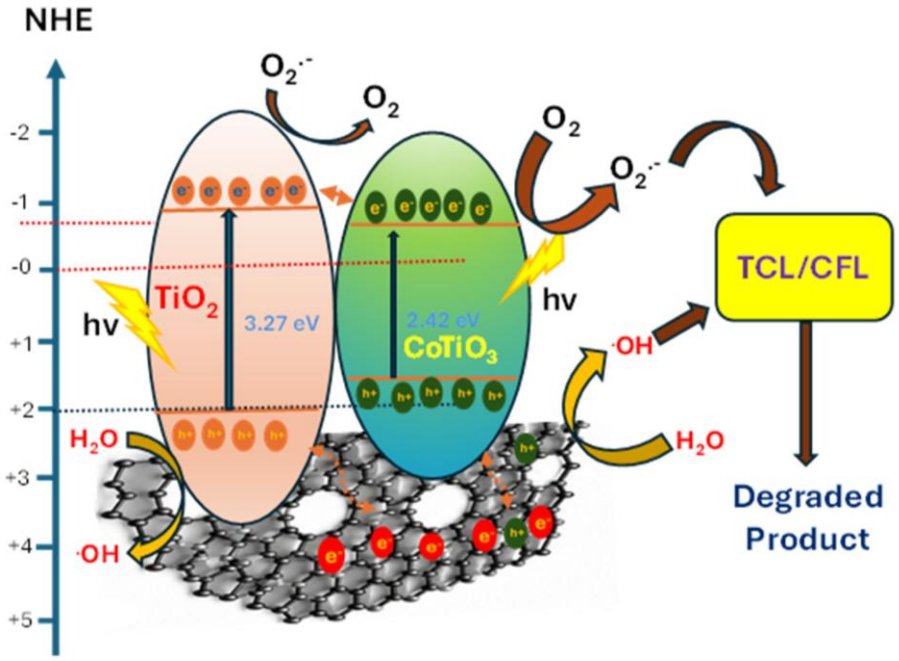


Fig. 11. Proposed photocatalytic mechanism of the HGN–$CoTiO_3$/TiO_2 heterostructure under UV irradiation and its role in the self-cleaning behaviour of HGN–$CoTiO_3$/TiO_2/PVDF membrane.

Upon UV irradiation, photogenerated electron-hole pairs are generated within the $CoTiO_3$/TiO_2 heterostructure. The conductive HGN framework serves as an efficient electron-transport pathway, promoting rapid charge separation and suppressing electron–hole recombination, consistent with the PL, transient photocurrent, and EIS results. The photogenerated electrons migrate through the HGN network and subsequently react with dissolved oxygen to generate superoxide radicals ($\bullet O_2^-$), whereas the remaining photogenerated holes oxidize surface hydroxyl groups or water molecules to produce hydroxyl radicals (•OH). The reactive species trapping experiments

further demonstrated that $\bullet O_2^-$ radicals predominantly contributed to TCL degradation, whereas photogenerated holes (h^+) played a more significant role during CFL degradation. These results indicate that both radical-mediated and direct hole oxidation pathways participate in the photocatalytic degradation process, although their relative contributions depend on the molecular structure of the target antibiotic. When incorporated into the PVDF membrane, the HGN–$CoTiO_3/TiO_2$ heterostructure simultaneously promotes antibiotic degradation and oxidation of adsorbed organic foulants under UV irradiation. Consequently, the embedded photocatalyst contributes to membrane self-cleaning, permeability recovery, and improved filtration performance.

Conclusion

This study demonstrates the successful development of a ternary heterostructured HGN–$CoTiO_3/TiO_2$ nanocomposite photocatalyst synthesized via hydrothermal treatment, where holey graphene functions as both a structural scaffold and conductive co-catalyst. The optimized HGN–$CoTiO_3/TiO_2$-30 (30 wt.% HGN) exhibited outstanding photocatalytic performance, achieving 99% removal of TCL and 96% removal of CFL from antibiotic-laden hospital wastewater under UV irradiation within 2 h. The enhanced activity is attributed to synergistic interactions between $CoTiO_3$ and TiO_2, facilitated by the high-surface-area and conductive framework of HGN, which promotes efficient charge separation, suppresses recombination, and increases the density of accessible active sites. Beyond powder photocatalysis, the nanocomposite was successfully integrated into self-cleaning hybrid ultrafiltration membranes. The membrane containing 2 wt.% HGN–$CoTiO_3/TiO_2$-30 (MTG2) exhibited improved hydrophilicity, increased negative surface charge, and robust mechanical stability, enabling 98% humic acid rejection and 98% TCL photodegradation under UV irradiation for 3 h. Enhanced self-cleaning efficiency at higher nanocomposite loading further demonstrates the antifouling potential and reusability of the hybrid membranes. By integrating adsorption, photocatalysis, and membrane separation within a single platform and validating performance in real hospital wastewater, this work advances the development of multifunctional treatment strategies for antibiotic-contaminated effluents. Future investigations should focus on visible-light activation, continuous-flow operation, and pilot-scale membrane module integration to further assess long-term stability and practical deployment in advanced wastewater treatment systems.

Data Availability

The raw and processed data required to reproduce the results of our work are available upon reasonable request.

Declaration of Competing Interest

The authors declare that they have no known competing financial interests or personal relationships that could have appeared to influence the work reported in this paper.

Acknowledgements

The authors express their gratitude to Khalifa University of Science and Technology (Abu Dhabi, UAE) for its support.

Funding

This research was funded by the Research and Innovation Center for Graphene and 2D Materials (RIC-2D), Khalifa University of Science and Technology (Abu Dhabi, UAE), under Directed Project Grant No. 8434000505. Additional support was provided by the Center for Membranes and Advanced Water Technology (KU-CMAT), Khalifa University of Science and Technology.

Author Contributions

Mahendra Kumar: Conceptualization. Methodology, Investigation, Data Analysis, Writing-Reviewing and Editing, Validation. Mohammad Faraz: Methodology, Data Analysis, Writing-Reviewing and Editing, Validation. Hanaa Hegab: Supervision, Reviewing and Editing, Validation. Aya F. Aboukhater: Methodology, Data Analysis, Writing-Reviewing and Editing. Mariam Ouda: Data Analysis, Writing-Reviewing and Editing. Habiba Alsafar: Supervision, Reviewing and Editing, Validation. Rahul N. Nair: Reviewing and Editing, Validation. Shadi W. Hasan: Conceptualization, Methodology, Reviewing and Editing, Supervision, Validation, Resources, Project Administration.

References

1 Wang, J., Li, F., Bao, Y. & Zhan, S. A Mini Review on the Synthesis of Mesoporous Silica and its Application in Antibiotic Removal. *Advanced Sustainable Systems* **9**, 2400634, doi:https://doi.org/10.1002/adsu.202400634 (2025).

2 Zhang, Q., Zheng, D., Bai, B., Ma, Z. & Zong, S. Insight into antibiotic removal by advanced oxidation processes (AOPs): Performance, mechanism, degradation pathways, and ecotoxicity assessment. *Chemical Engineering Journal* **500**, 157134, doi:https://doi.org/10.1016/j.cej.2024.157134 (2024).

3 Silerio-Vázquez, F. d. J., González-Burciaga, L. A., Antileo, C., Núñez-Núñez, C. M. & Proal-Nájera, J. B. Photocatalytic degradation of antibiotics in water via TiO2-x: Research needs for technological advancements. *Journal of Hazardous Materials Advances* **16**, 100506, doi:https://doi.org/10.1016/j.hazadv.2024.100506 (2024).

4 Onkani, S. P., Akpotu, S. O., Diagboya, P. N., Mtunzi, F. & Osabohien, E. Enhanced Aqueous Photo-Degradation of Ciprofloxacin and Tetracycline Using Ag-Decorated ZnO Plasmonic Catalyst. *ACS Sustainable Resource Management* **1**, 2294-2303, doi:10.1021/acssusresmgt.4c00318 (2024).

5 Cai, Z. *et al.* Hypercrosslinking porous polymer layers on TiO2-graphene photocatalyst: Enhanced adsorption of water pollutants for efficient degradation. *Water Research* **227**, 119341, doi:https://doi.org/10.1016/j.watres.2022.119341 (2022).

6 Han, C.-H. *et al.* Oxidation of tetracycline and oxytetracycline for the photo-Fenton process: Their transformation products and toxicity assessment. *Water Research* **172**, 115514, doi:https://doi.org/10.1016/j.watres.2020.115514 (2020).

7 Sha, S. *et al.* In-situ removal of residual antibiotics (enrofloxacin) in recirculating aquaculture system: effect of ultraviolet photolysis plus biodegradation using immobilized microbial granules. *Journal of Cleaner Production* **333**, doi:10.1016/j.jclepro.2021.130190 (2022).

8 Tang, J. *et al.* Recent advancements in antibiotics removal by bio-electrochemical systems (BESs): From mechanisms to application of emerging combined systems. *Water Research* **268**, 122683, doi:https://doi.org/10.1016/j.watres.2024.122683 (2025).

9 Hazra, M., Watts, J. E. M., Williams, J. B. & Joshi, H. An evaluation of conventional and nature-based technologies for controlling antibiotic-resistant bacteria and antibiotic-resistant genes in wastewater treatment plants. *Science of The Total Environment* **917**, 170433, doi:https://doi.org/10.1016/j.scitotenv.2024.170433 (2024).

10 Jiang, Y. *et al.* Lead-Free Cs2AgBiBr6/TiO2 S-Scheme Heterojunction for Efficient Photocatalytic Antibiotic Rifampicin Degradation. *Nano Letters* **24**, 12597-12604, doi:10.1021/acs.nanolett.4c03648 (2024).

11 Payan, A., Akbar Isari, A. & Gholizade, N. Catalytic decomposition of sulfamethazine antibiotic and pharmaceutical wastewater using Cu-TiO2@functionalized SWCNT ternary porous nanocomposite: Influential factors, mechanism, and pathway studies. *Chemical Engineering Journal* **361**, 1121-1141, doi:https://doi.org/10.1016/j.cej.2018.12.118 (2019).

12 Yu, X. *et al.* Photocatalytic degradation of ciprofloxacin using Zn-doped Cu2O particles: Analysis of degradation pathways and intermediates. *Chemical Engineering Journal* **374**, 316-327, doi:https://doi.org/10.1016/j.cej.2019.05.177 (2019).

13 Li, S., Tian, Y. & Zhang, G. Modification of porous bismuth molybdate for high removal of antibiotics and H2O2 production. *Catalysis Science & Technology* **14**, 6420-6429, doi:10.1039/d4cy00906a (2024).
14 Zhou, S. *et al.* Oxygen Vacancies Modified TiO2/O-Terminated Ti3C2 Composites: Unravelling the Dual Effects between Oxygen Vacancy and High-Work-Function Titanium Carbide. *Advanced Functional Materials* **33**, 2307702, doi:https://doi.org/10.1002/adfm.202307702 (2023).
15 Jin, Y., Mi, X., Qian, J., Ma, N. & Dai, W. CdS Nanoparticles Supported on a Dual Metal–Organic Framework as a Catalyst for the Photodegradation of Tetracycline. *ACS Applied Nano Materials* **7**, 3154-3167, doi:10.1021/acsanm.3c05511 (2024).
16 Han, T. *et al.* Hierarchical FeTiO3–TiO2 hollow spheres for efficient simulated sunlight-driven water oxidation. *Nanoscale* **7**, 15924-15934, doi:10.1039/c5nr05242d (2015).
17 Lin, B., Li, S., Peng, Y., Chen, Z. & Wang, X. MOF-derived core/shell C-TiO2/CoTiO3 type II heterojunction for efficient photocatalytic removal of antibiotics. *Journal of Hazardous Materials* **406**, 124675, doi:https://doi.org/10.1016/j.jhazmat.2020.124675 (2021).
18 Wang, L. *et al.* A visible light driven 3D hierarchical CoTiO3/BiOBr direct Z-scheme heterostructure with enhanced photocatalytic degradation performance. *New Journal of Chemistry* **46**, 124-135, doi:10.1039/d1nj04252a (2022).
19 Xing, C. *et al.* Porous NiTiO3/TiO2 nanostructures for photocatatalytic hydrogen evolution. *Journal of Materials Chemistry A* **7**, 17053-17059, doi:10.1039/c9ta04763h (2019).
20 Wei, F. *et al.* Rational Construction of MOF-Derived Porous ZnTiO3/TiO2 Heterostructured Photocatalysts with Remarkable Photocatalytic Performance. *ACS Omega* **8**, 41765-41772, doi:10.1021/acsomega.3c06307 (2023).
21 Reza Amani-Ghadim, A. *et al.* Development of a novel Z-scheme CoxNi1−xTiO3/CdS (x = 0.5) photocatalyst for the efficient degradation of organic pollutants via a visible-light-driven photocatalytic process. *Journal of Colloid and Interface Science* **663**, 1035-1051, doi:https://doi.org/10.1016/j.jcis.2024.03.005 (2024).
22 Xia, Z. *et al.* Visible-Light Photocatalytic Degradation Efficiency of Tetracycline and Rhodamine B Using a Double Z-Scheme Heterojunction Catalyst of UiO-66-NH2/BiOCl/Bi2S3. *Inorganic Chemistry* **63**, 14578-14590, doi:10.1021/acs.inorgchem.4c01917 (2024).
23 Ding, P. *et al.* Visible-light degradation of antibiotics catalyzed by titania/zirconia/graphitic carbon nitride ternary nanocomposites: a combined experimental and theoretical study. *Applied Catalysis B: Environmental* **300**, 120633, doi:https://doi.org/10.1016/j.apcatb.2021.120633 (2022).
24 Potbhare, A. K. *et al.* Bioinspired graphene-based metal oxide nanocomposites for photocatalytic and electrochemical performances: an updated review. *Nanoscale Advances* **6**, 2539-2568, doi:10.1039/d3na01071f (2024).
25 Yang, T., Gao, T., Fan, J. & Zhang, L. High-efficiency treatment of antibiotic wastewater by a self-assembled coated double-heterojunction TiO2/g-C3N4/BN photocatalyst. *New Journal of Chemistry* **48**, 17350-17359, doi:10.1039/d4nj02761b (2024).
26 Zhao, W., Duan, J., Ji, B., Ma, L. & Yang, Z. Novel formation of large area N-TiO2/graphene layered materials and enhanced photocatalytic degradation of

antibiotics. *Journal of Environmental Chemical Engineering* **8**, 102206, doi:https://doi.org/10.1016/j.jece.2018.02.014 (2020).
27 Cui, Y. *et al.* Fabrication of silver vanadate quantum dots/reduced graphene oxide/graphitic carbon nitride Z-scheme heterostructure modified polyvinylidene fluoride self-cleaning membrane for enhancing photocatalysis and mechanism insight. *Journal of Colloid and Interface Science* **614**, 677-689, doi:https://doi.org/10.1016/j.jcis.2022.01.008 (2022).
28 Yang, C. *et al.* Ultrathin g-C3N4 composite Bi2WO6 embedded in PVDF UF membrane with enhanced permeability, anti-fouling performance and durability for efficient removal of atrazine. *Journal of Hazardous Materials* **451**, 131154, doi:https://doi.org/10.1016/j.jhazmat.2023.131154 (2023).
29 Zhou, P. *et al.* Construction of PES mixed matrix membranes incorporating ZnFe2O4 @MXene composites with high permeability and antifouling performance. *Journal of Environmental Chemical Engineering* **11**, 110252, doi:https://doi.org/10.1016/j.jece.2023.110252 (2023).
30 Xu, J.-F. *et al.* Ag@SnS/PVDF membranes with self-cleaning ability driven by photocatalysis process. *Journal of Membrane Science* **707**, 123015, doi:https://doi.org/10.1016/j.memsci.2024.123015 (2024).
31 Lin, Y., Plaza-Rivera, C. O., Hu, L. & Connell, J. W. Scalable Dry-Pressed Electrodes Based on Holey Graphene. *Accounts of Chemical Research* **55**, 3020-3031, doi:10.1021/acs.accounts.2c00457 (2022).
32 Qu, Y., Zhou, W. & Fu, H. Porous Cobalt Titanate Nanorod: A New Candidate for Visible Light-Driven Photocatalytic Water Oxidation. *ChemCatChem* **6**, 265-270, doi:https://doi.org/10.1002/cctc.201300718 (2014).
33 Wei, S. *et al.* Enhanced Hydrogen Storage Properties of LiAlH4 by Excellent Catalytic Activity of XTiO3@h-BN (X = Co, Ni). *Advanced Functional Materials* **32**, 2110180, doi:https://doi.org/10.1002/adfm.202110180 (2022).
34 Gao, Z. *et al.* Pt Nanoparticles Supported on Iron and Nitrogen-Doped Holey Graphene for Boosting ORR Performance. *ACS Applied Nano Materials* **6**, 10521-10530, doi:10.1021/acsanm.3c01502 (2023).
35 Wyss, K. M., Chen, W., Beckham, J. L., Savas, P. E. & Tour, J. M. Holey and Wrinkled Flash Graphene from Mixed Plastic Waste. *ACS Nano* **16**, 7804-7815, doi:10.1021/acsnano.2c00379 (2022).
36 Guo, H. *et al.* Enhanced photocatalytic CO2 reduction over direct Z-scheme NiTiO3/g-C3N4 nanocomposite promoted by efficient interfacial charge transfer. *Chemical Engineering Journal* **412**, 128646, doi:https://doi.org/10.1016/j.cej.2021.128646 (2021).
37 Ye, R. *et al.* Fabrication of CoTiO3/g-C3N4 Hybrid Photocatalysts with Enhanced H2 Evolution: Z-Scheme Photocatalytic Mechanism Insight. *ACS Applied Materials & Interfaces* **8**, 13879-13889, doi:10.1021/acsami.6b01850 (2016).
38 Ramírez-Ortega, D. *et al.* Exploring the photocatalytic production of hydrogen by Co, Cu or Pd species as co-catalysts supported on a ZnxTiyOz perovskite/TiO2 structure. *International Journal of Hydrogen Energy* **89**, 1135-1148, doi:https://doi.org/10.1016/j.ijhydene.2024.09.420 (2024).
39 Zhang, L. *et al.* Effective charge separation and enhanced photocatalytic activity by the heterointerface in MoS2/reduced graphene oxide composites. *RSC Advances* **6**, 60318-60326, doi:10.1039/c6ra10923c (2016).
40 Singh, J., Nguyen, D. D., Leclere, P. & Nguyen-Tri, P. Recent Advancements in Graphene-Based Nanocomposites for Enhanced Photocatalysis in Environmental

Remediation: A Comprehensive Review. *Reviews of Environmental Contamination and Toxicology* **263**, 13, doi:10.1007/s44169-025-00086-4 (2025).
41 Wang, Y. *et al.* Amino-Assisted NH2-UiO-66 Anchored on Porous g-C3N4 for Enhanced Visible-Light-Driven CO2 Reduction. *ACS Applied Materials & Interfaces* **11**, 30673-30681, doi:10.1021/acsami.9b04302 (2019).
42 Wang, R. *et al.* Modulation of Trivalent/Tetravalent Metallic Elements in Ni-Based Layered Double Hydroxides for Photocatalytic CO2 Reduction. *ACS Applied Materials & Interfaces* **14**, 35654-35662, doi:10.1021/acsami.2c07940 (2022).
43 Li, Y. *et al.* Achieving Controllable CoTiO3-Encapsulated TiO2 Heterostructures for Enhanced Photoelectrochemical Water Splitting. *ACS Applied Energy Materials* **2**, 8229-8235, doi:10.1021/acsaem.9b01694 (2019).
44 Xu, Z. *et al.* Photocatalytic antifouling PVDF ultrafiltration membranes based on synergy of graphene oxide and TiO2 for water treatment. *Journal of Membrane Science* **520**, 281-293, doi:https://doi.org/10.1016/j.memsci.2016.07.060 (2016).
45 Nawaz, H. *et al.* Photodegradation of textile pollutants by nanocomposite membranes of polyvinylidene fluoride integrated with polyaniline–titanium dioxide nanotubes. *Chemical Engineering Journal* **419**, 129542, doi:https://doi.org/10.1016/j.cej.2021.129542 (2021).
46 Zhang, J. *et al.* Ag@BiOBr/PVDF photocatalytic membrane for remarkable BSA anti-fouling performance and insight of mechanism. *Journal of Membrane Science* **677**, 121611, doi:https://doi.org/10.1016/j.memsci.2023.121611 (2023).
47 Li, Y. *et al.* Ultrafiltration membrane modified via synergistic integration of quaternary ammonium compounds bactericidal activity and g-C3N4 photocatalysis: Toward superior antibiofouling and self-cleaning property. *Chemical Engineering Journal* **499**, 156207, doi:https://doi.org/10.1016/j.cej.2024.156207 (2024).
48 Yang, C. *et al.* Photocatalytic PVDF ultrafiltration membrane blended with visible-light responsive Fe(III)-TiO2 catalyst: Degradation kinetics, catalytic performance and reusability. *Chemical Engineering Journal* **417**, 129340, doi:https://doi.org/10.1016/j.cej.2021.129340 (2021).
49 Zhou, C. *et al.* Explication of polydopamine modified g-C3N4 as effective additive in PVDF nanocomposite membrane fabrication for enhanced ultrafiltration and self-cleaning performance. *Journal of Environmental Chemical Engineering* **11**, 110577, doi:https://doi.org/10.1016/j.jece.2023.110577 (2023).
50 Shao, B. *et al.* Nitrogen-Doped Hollow Mesoporous Carbon Spheres Modified g-C3N4/Bi2O3 Direct Dual Semiconductor Photocatalytic System with Enhanced Antibiotics Degradation under Visible Light. *ACS Sustainable Chemistry & Engineering* **6**, 16424-16436, doi:10.1021/acssuschemeng.8b03480 (2018).
51 Yuan, X. *et al.* Design of core-shelled g-C3N4@ZIF-8 photocatalyst with enhanced tetracycline adsorption for boosting photocatalytic degradation. *Chemical Engineering Journal* **416**, 129148, doi:https://doi.org/10.1016/j.cej.2021.129148 (2021).
52 Ma, Y., He, D., Liu, Q., Le, S. & Wang, X. A S-type 2D/2D heterojunction via intercalating ultrathin g-C3N4 into NH4V4O10 nanosheets and the boosted removal of ciprofloxacin. *Applied Catalysis B: Environment and Energy* **344**, 123642, doi:https://doi.org/10.1016/j.apcatb.2023.123642 (2024).
53 Kumar, M. *et al.* Polydopamine-coated graphene oxide nanosheets embedded in sulfonated poly(ether sulfone) hybrid UF membranes with superior antifouling

properties for water treatment. *Chemical Engineering Journal* **433**, 133526, doi:https://doi.org/10.1016/j.cej.2021.133526 (2022).

54 Yang, F. *et al.* Self-cleaning, antimicrobial, and antifouling membrane via integrating mesoporous graphitic carbon nitride into polyvinylidene fluoride. *Journal of Membrane Science* **606**, 118146, doi:https://doi.org/10.1016/j.memsci.2020.118146 (2020).

55 Chen, Z. *et al.* Photocatalytic antifouling properties of novel PVDF membranes improved by incorporation of SnO2-GO nanocomposite for water treatment. *Separation and Purification Technology* **259**, 118184, doi:https://doi.org/10.1016/j.seppur.2020.118184 (2021).

Supplementary Files

This is a list of supplementary files associated with this preprint. Click to download.

- SupplementaryMaterialsOctober122026.docx